SANDIA REPORT

SAND2013-7434
Unlimited Release
Printed September 2013

Modeling Interfacial Fracture in Sierra

Arthur Brown, Yuki Ohashi, Wei-Yang Lu, Stacy Nelson, James Foulk III, Dave Reedy, Kevin Austin, and Steve Margolis

Prepared by
Sandia National Laboratories
Albuquerque, New Mexico 87185 and Livermore, California 94550

Sandia National Laboratories is a multi-program laboratory managed and operated by Sandia Corporation, a wholly owned subsidiary of Lockheed Martin Corporation, for the U.S. Department of Energy's National Nuclear Security Administration under contract DE-AC04-94AL85000.

Approved for public release; further dissemination unlimited.

Sandia National Laboratories

Issued by Sandia National Laboratories, operated for the United States Department of Energy by Sandia Corporation.

NOTICE: This report was prepared as an account of work sponsored by an agency of the United States Government. Neither the United States Government, nor any agency thereof, nor any of their employees, nor any of their contractors, subcontractors, or their employees, make any warranty, express or implied, or assume any legal liability or responsibility for the accuracy, completeness, or usefulness of any information, apparatus, product, or process disclosed, or represent that its use would not infringe privately owned rights. Reference herein to any specific commercial product, process, or service by trade name, trademark, manufacturer, or otherwise, does not necessarily constitute or imply its endorsement, recommendation, or favoring by the United States Government, any agency thereof, or any of their contractors or subcontractors. The views and opinions expressed herein do not necessarily state or reflect those of the United States Government, any agency thereof, or any of their contractors.

Printed in the United States of America. This report has been reproduced directly from the best available copy.

Available to DOE and DOE contractors from
U.S. Department of Energy
Office of Scientific and Technical Information
P.O. Box 62
Oak Ridge, TN 37831

Telephone: (865) 576-8401
Facsimile: (865) 576-5728
E-Mail: reports@adonis.osti.gov
Online ordering: http://www.osti.gov/bridge

Available to the public from
U.S. Department of Commerce
National Technical Information Service
5285 Port Royal Rd.
Springfield, VA 22161

Telephone: (800) 553-6847
Facsimile: (703) 605-6900
E-Mail: orders@ntis.fedworld.gov
Online order: http://www.ntis.gov/help/ordermethods.asp?loc=7-4-0#online

SAND2013-7434
Unlimited Release
Printed September 2013

Modeling Interfacial Fracture in Sierra

Arthur Brown, Yuki Ohashi, Wei-Yang Lu, Stacy Nelson, James Foulk III,
Dave Reedy, Kevin Austin, and Steve Margolis
Multi-physics Modeling and Simulation
Sandia National Laboratories
P.O. Box 969
Livermore, CA 94551-0969

Abstract

This report summarizes computational efforts to model interfacial fracture using cohesive zone models in the SIERRA/SolidMechanics (SIERRA/SM) finite element code. Cohesive surface elements were used to model crack initiation and propagation along predefined paths. Mesh convergence was observed with SIERRA/SM for numerous geometries. As the funding for this project came from the Advanced Simulation and Computing Verification and Validation (ASC V&V) focus area, considerable effort was spent performing verification and validation. Code verification was performed to compare code predictions to analytical solutions for simple three-element simulations as well as a higher-fidelity simulation of a double-cantilever beam. Parameter identification was conducted with Dakota using experimental results on asymmetric double-cantilever beam (ADCB) and end-notched-flexure (ENF) experiments conducted under Campaign-6 funding. Discretization convergence studies were also performed with respect to mesh size and time step and an optimization study was completed for mode II delamination using the ENF geometry. Throughout this verification process, numerous SIERRA/SM bugs were found and reported, all of which have been fixed, leading to over a 10-fold increase in convergence rates. Finally, mixed-mode flexure experiments were performed for validation.

One of the unexplained issues encountered was material property variability for ostensibly the same composite material. Since the variability is not fully understood, it is difficult to accurately assess uncertainty when performing predictions.

ACKNOWLEDGEMENTS

The authors would like to thank Tom Bennett and Jim McElhanon for sample preparation, Dave Reedy for experimental advice, and Monica Martinez-Canales for advice on uncertainty quantification.

CONTENTS

Acknowledgements 4

1. Introduction 7
   1.1 Executive Summary 7

2. Verification 9
   2.1. Mode I 9
   2.2. Mode II 10
   2.3. Double-cantilever beam 10

3. Modeling and Experiments 13
   3.1. Bulk testing 13
   3.2. Asymmetric double-cantilever beam 15
      3.2.1. Optimization 16
      3.2.2. Discretization verification 17
   3.3. End-notched flexure 18
      3.3.1. Sensitivity analysis 21
   3.4. ADCB Tests revisited 24
   3.5. High-rate ADCB 25
   3.6. Rising Resistance Curve 26
   3.7. Validation with Mixed-Mode Flexure 30

4. Summary and Conclusions 33

5. References 35

6. Appendix 37

Distribution 39

FIGURES

Figure 1: Three-element code verification simulation. 9
Figure 2: Traction-separation response. 9
Figure 3: Error in traction and displacement. 10
Figure 4: Code verification DCB geometry. 11
Figure 5: DCB code verification results. 11
Figure 6. Composite tensile specimen design (8” x 1” x 0.04”). 14
Figure 7. Stress-strain response of the graphite and glass specimens. 14
Figure 8. The transparency of the glass specimens decreased after the change in slope in the stress-strain response. 15
Figure 9: Experimental specimen and fixturing for ADCB. 16
Figure 10: Comparison between simulation and experiment for ADCB. 16
Figure 11: Solution verification for ADCB simulations. 17
Figure 12: Time discretization convergence study. 18
Figure 13: ENF specimen and fixturing. 19
Figure 14: Simulation compared to experiment for ENF. 19

Figure 15: Simulation deflection of ENF geometry. 19
Figure 16: Simulation compared to experiment for ENF. 20
Figure 17: Mesh convergence study for the ENF simulation. 20
Figure 18: ENF simulation results from the sensitivity analysis. 21
Figure 19: Depiction of the quality of the fit for Equation (3). 24
Figure 20: The high-rate ADCB specimen during the fracture test. 25
Figure 21: The high-rate simulation showing crack propagation. 26
Figure 22: The crack length evolution from simulation and experiment. 26
Figure 23: ADCB response without precracking. 27
Figure 24: In some ADCB specimens, a secondary crack appeared ahead of the interface crack. The secondary cracks always occurred as delamination between carbon plies. 27
Figure 25: The resistance curve based on Equation (4). 28
Figure 26: Load-displacement response using the R-curve in Figure 25. 28
Figure 27: Response curves for the cases where the interply toughness is less than (150 J/m^2) or equal to (250 J/m^2) the interface toughness between the two materials. 29
Figure 28: Displacements (magnified by 10) at the corresponding peak loads for the cases where the interply toughness is less than (150 J/m^2) or equal to (250 J/m^2) the interface toughness between the two materials. 29
Figure 29: Mixed-mode flexure geometry. 30
Figure 30: Thouless-Parmigiani model results. 31
Figure 31: Epistemic uncertainty bounds predicted through simulation, compared with experimental results. 31
Figure 32: Mixed-mode flexure results for 580 J/m^2. 32
Figure 33: Mixed-mode flexure results for 700 J/m^2. 32

TABLES

Table 1. Material properties 15
Table 2. Correlation table from sensitivity analysis. 23
Table 3: Nominal values and associated uncertainties for the ENF parameters. 24

1. INTRODUCTION

Composite materials are prominent in many applications, such as aircraft, fuel tanks, and wind turbine blades. The structural integrity of laminates or joints can be compromised by interfacial failure, which can occur between plies (delamination) or at bonded joints. These types of failure can occur due to thermal and/or mechanical loading that induce normal and/or shear stresses at the interfaces. For this reason, a method of predicting interfacial failure with confidence is important in composite design.

One method of simulating failure with the finite element method is using cohesive zone models. These models prescribe traction-separation relations for the behavior of cohesive surface elements, which are collapsed hexahedra that reside at the interface between two surfaces. These elements can be used to model crack initiation and propagation along predefined paths, or can be adaptively inserted when some criteria is met to allow propagation in other directions. The main advantages of the cohesive zone method over other methods of modeling failure are that both crack initiation and propagation can be modeled, and that the predictions are very insensitive to mesh size.

1.1 Executive Summary

This report summarizes computational efforts to model brittle interfacial fracture using cohesive zone models in the SIERRA/SolidMechanics (SIERRA/SM) implicit finite element code. One of the primary benefits in using cohesive surface elements to model fracture is that they regularize the solution to alleviate the dependence on mesh size and it will be demonstrated that mesh convergence was observed with SIERRA/SM for numerous geometries.

Various cohesive zone models exist in the literature, including Xu-Needleman [1], Tvergaard-Hutchinson [2], and Thouless-Parmigiani [3]. In this work, the latter two models were exercised. The advantage of the Thouless-Parmigiani model is that different critical energy release rates can be specified for mode I and mode II. Unfortunately, this added complexity to the solution and prevented the SIERRA/SM quasistatic solver from consistently reaching convergence, so most of the results presented use the Tvergaard-Hutchinson model.

Although the traction-separation law varies for these different models, the general behavior is that the traction increases to a maximum and then decreases to zero as the separation increases. During this process, the energy dissipated is equal to the critical energy release rate and its determination is crucial to analyze designs. Typical methods of determining the critical energy release rate are through experiments, such as the double-cantilever beam (DCB) for mode I, end-notched flexure (ENF) for mode II, and mixed-mode flexure (MMF) for mixed mode. These types of experiments have been modeled by a number of authors. Most use symmetric, single-material specimen geometries: de Moura [4] modeled ENF but did not compare the results with experiments; Iannucci [5] performed dynamic simulations for DCB, ENF, and MMB specimens, but only compared the DCB simulations to experimental results; and Mi et al. [6] modeled quasistatic DCB, ENF, and MMB tests, but only compared the DCB simulations to experimental results. Liu et al. [7] used a bimaterial ENF specimen, and compared asymmetric double-cantilever beam (ADCB) simulations to experimental results, but no comparison between

experiment and analysis was made for the ENF geometry. In this effort, ADCB, ENF, and MMB geometries are simulated and compared to the experimental results of Lu [8].

As the funding for this project came from the ASC V&V focus area, considerable effort was spent performing verification and validation. Code verification was performed to compare code predictions to analytical solutions for simple three-element simulations as well as a higher-fidelity simulation of a double-cantilever beam. Parameter identification was completed with the experimental results of ADCB and ENF experiments conducted under Campaign-6 funding. These results were used to complete a characterization that was performed with Dakota to optimize the interlaminar fracture toughness in the ADCB simulations. These parameters were then applied to ENF simulations, and good agreement was obtained with the experimental results. For one of the ENF geometries, Dakota was used to run a Latin Hypercube Sampling (LHS) sensitivity study with 37 geometric and material property parameters. Two response functions were calculated from the results and correlation matrices and scatter plots were generated using JMP software. Also, a high-rate asymmetric double-cantilever beam simulation was completed with SIERRA/SM transient dynamics capabilities and compared with experimental results. The critical energy release rate resulting from this experiment was found to be lower than that of the quasistatic test. The effects of temperature were included in these simulations, as specimens were composed of multiple materials and residual stresses due to a coefficient of thermal expansion (CTE) mismatch would sometimes be induced through the curing process. During this process numerous SIERRA/SM bugs were found and reported, all of which have been fixed, leading to over a 10-fold increase in convergence rates.

Lastly, validation was performed using a mixed mode flexure geometry and experimental results. Error propagation was performed to study the effects of parameter uncertainties on the validation metric. The cohesive zone capability in SIERRA/SM was then used to investigate the possibility of failure in adhesively bonded joints, as documented in Brown and English [9].

2. VERIFICATION

In order to verify that the cohesive zone model implementation is correct, the first step was to check that Adagio, the SIERRA/SM implicit code, was calculating and reporting the correct cohesive tractions and displacements. Code verification was performed with simple three-element models as well as a higher-fidelity simulation of a double-cantilever beam geometry.

2.1. Mode I

Figure 1 describes a three-element simulation to check the mode I accuracy. Two rigid blocks are connected by a cohesive layer and pulled apart in tension. The simulated traction-separation results are shown in Figure 2. By comparing these results to the desired traction-separation relation based on the parameters used, the errors can be plotted as a function of simulation time (see Figure 3). These errors were found to be acceptable.

Figure 1: Three-element code verification simulation.

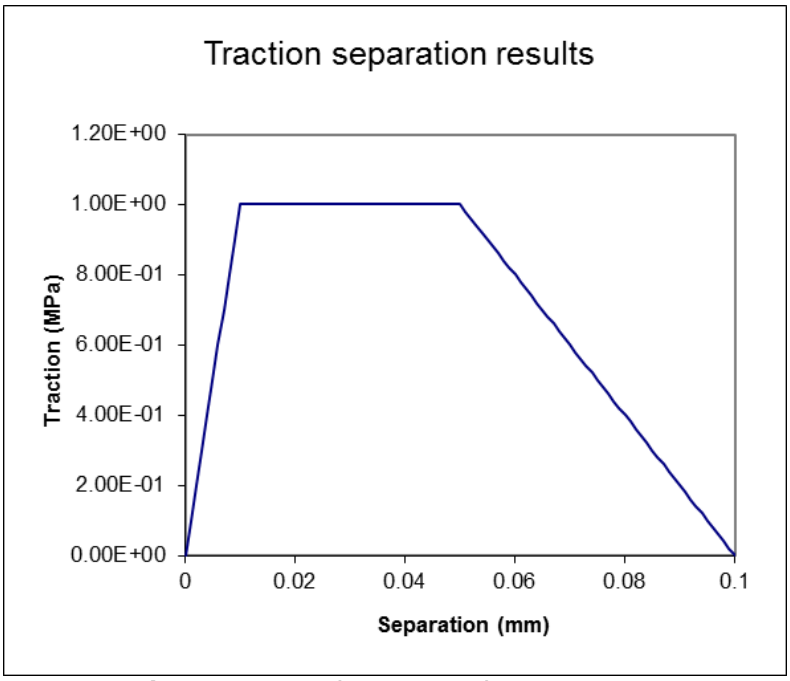

Figure 2: Traction-separation response.

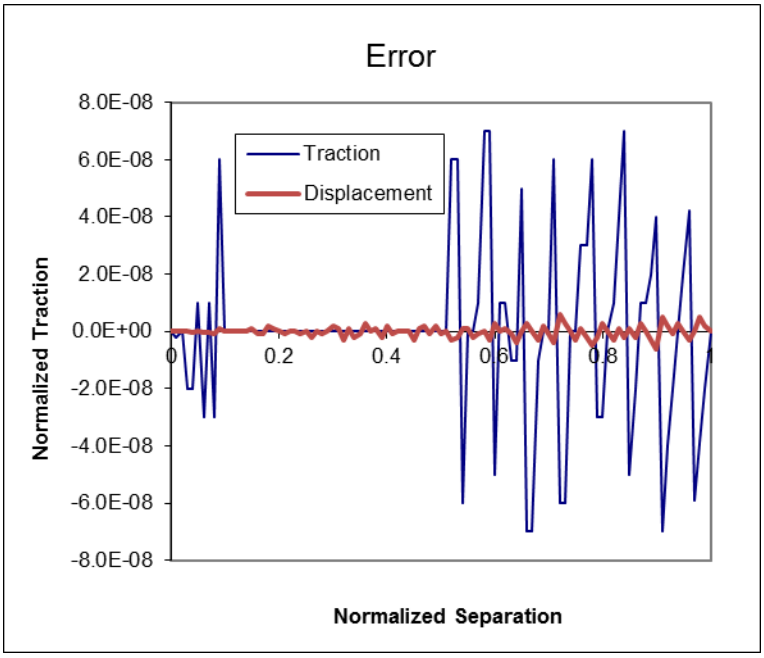

Figure 3: Error in traction and displacement.

2.2. Mode II

To check that the implementation was also capable of modeling mode II failure, the boundary conditions on the model in Figure 1 were modified such that the top block was displaced horizontally relative to the bottom block. The results were very similar to those displayed in Figure 2 and Figure 3, and the errors were found to be within reason.

2.3. Double-cantilever beam

The implementation was also verified with a higher fidelity model through comparison with an analytical solution based on beam theory. For a double-cantilever beam (DCB) being pulled apart at one end (see Figure 4), the crack should propagate according to the following relation [10]

$$c = \left(\frac{3Ed^2b^3}{4G_c} \right)^{1/4}, \tag{1}$$

where c is the crack length, E is Young's modulus of the beams, d is the opening displacement, b is the beam height, and G_c is the interlaminar fracture toughness.

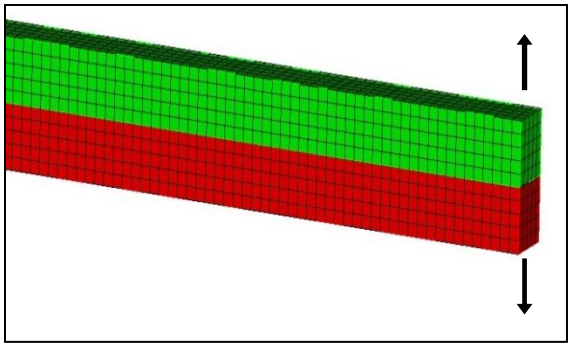

Figure 4: Code verification DCB geometry.

The higher fidelity model for comparison with the analytical solution is shown in Figure 4. This model, which was created with a beam height of 1 mm, a beam material modulus of 6,900 MPa, and a critical energy release rate of 500 J/m^2 at the cohesive zone, consists of 12,500 hexahedral elements with 1,250 cohesive surface elements between the two beams. A simulation was performed on this mesh in which the top and bottom beams were pulled apart to a final opening of 2 mm at the beam ends. For the purposes of comparing the simulated crack length to the analytical solution, the crack tip was defined as the location where the cohesive zone separation is at 10% of the critical value, similar to what was done in [11]. In Figure 5, the results from the Adagio analysis are shown compared with the theoretical solution in equation (1). This gives further confidence in the Adagio implementation of the cohesive zone models.

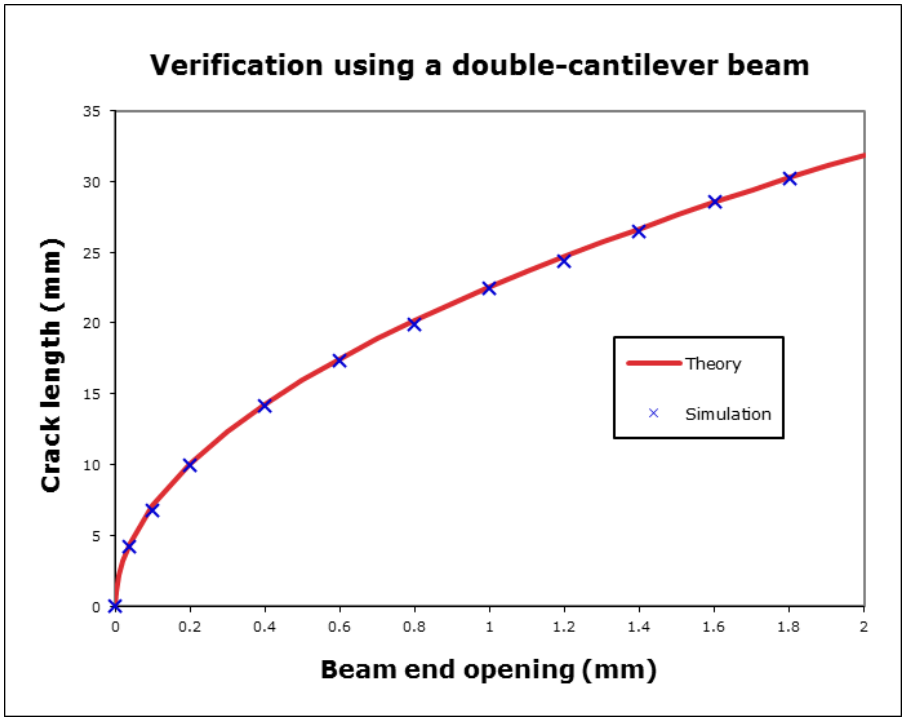

Figure 5: DCB code verification results.

3. MODELING AND EXPERIMENTS

3.1. Bulk testing

The ADCB, ENF, and MMF specimens for experimentation and modeling were manufactured from woven E-glass and graphite pre-impregnated materials. Pre-impregnated materials, or "pre-pregs," are composite material in which the reinforcing fibers are "pre-impregnated" with the matrix material, which is usually an epoxy resin. To allow for handling, sheets of pre-preg materials are usually partially cured and then stored as rolls in cold temperatures to delay complete curing. The specific materials used for this study were a 3k woven E-glass (Hexcel 7781, 8-harness satin weave with a UF3362 TCR resin system) and a 1k woven graphite (Toray T-300, 5-harness satin weave with a UF3360 TCR resin system) These materials were initially characterized to determine the relevant orthotropic material properties using a combination of experimental results, micromechanics, and engineering judgment (see Brown et al. [12]). For each composite material, tensile specimens consisting of five plies were manufactured with three different orientations: 0°, 45°, and 90° off the rolling axis. All specimens were fabricated with Teflon-coated peel-ply and cured at 350 °F for one hour at 45 psi.

The 0° and 90° specimens were used to determine Young's moduli and Poisson's ratios (see ASTM D3039-76 in [13]), and the 45° specimens were used to calculate the in-plane shear moduli (see ASTM D3518 in [13]). An example of the specimen response is shown in Figure 7. For each material and material orientation, specimens were loaded and unloaded elastically multiple times at room temperature. The axial and transverse strains were measured with a strain gage (type CEA-06-250UT-350) mounted in the center of the gauge section (see Figure 6). The resulting property sets are shown in Table 1, where the notation 11 refers to the 0° direction, 22 is the 90° direction, and 33 is the out-of-plane direction. The stress-strain response for the graphite and glass specimens are shown in Figure 7. The glass specimen response had a bilinear form, believed to be due to microcracking. The transparency of the specimens visibly changed during testing, but only after the change in slope was observed (see Figure 8). The initial slope was used for the elastic properties. It was verified that the stress at which the slope changed was not reached in the fracture simulations for the ADCB, ENF, and MMB geometries.

The values of some of the bulk properties were estimated instead of experimentally determined due to the time and cost constraints. The purpose of the sensitivity analysis performed later in this study was in part to see if these parameters have a significant impact on the results, and if so, then to perform additional experiments to determine the values more accurately.

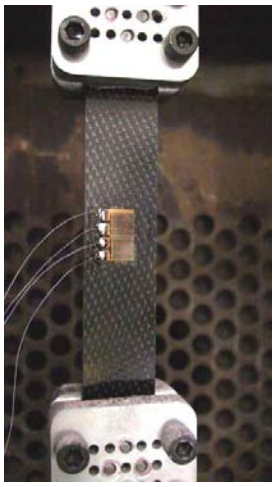

Figure 6. Composite tensile specimen design (8” x 1” x 0.04”).

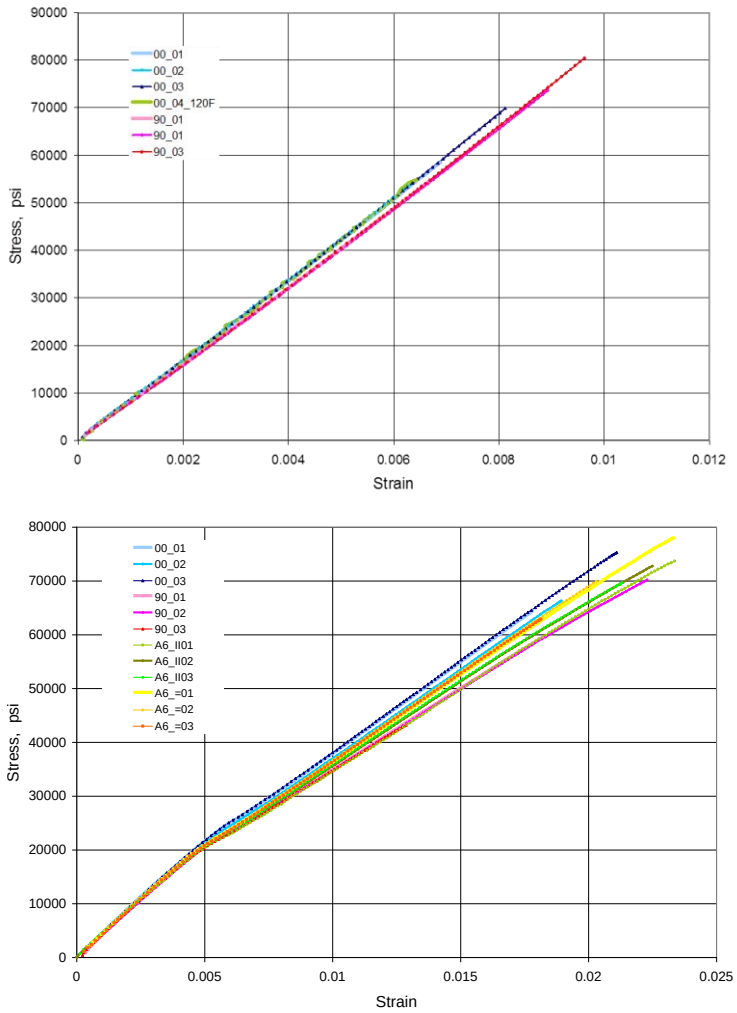

Figure 7. Stress-strain response of the graphite and glass specimens.

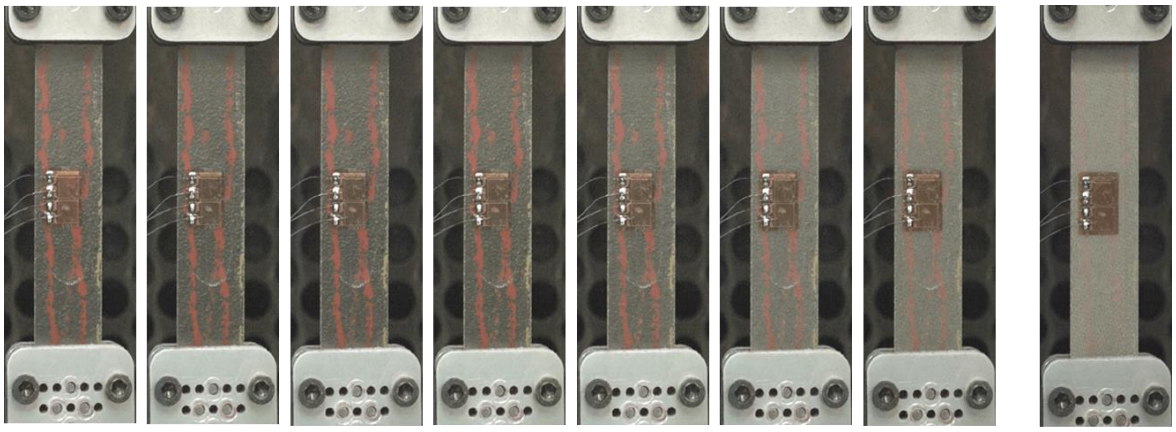

Figure 8. The transparency of the glass specimens decreased after the change in slope in the stress-strain response.

Table 1. Material properties

	Graphite	E-glass	Justification
Young's modulus 11 (GPa)	59	30	Measured value
Young's modulus 22 (GPa)	57	29	Measured value
Young's modulus 33 (GPa)	9.8	11	Micromechanics
Poisson's ratio 12	0.048	0.16	Measured value
Poisson's ratio 23	0.30	0.27	Micromechanics
Poisson's ratio 31	0.05	0.10	Micromechanics
Shear modulus 12 (GPa)	4.6	7.8	Measured value
Shear modulus 23 (GPa)	4.6	7.8	Estimate
Shear modulus 31 (GPa)	4.6	7.8	Estimate
CTE 11 ($°C^{-1}$)	1.e-6	8.e-6	Estimate
CTE 22 ($°C^{-1}$)	1.e-6	8.e-6	Estimate
CTE 33 ($°C^{-1}$)	3.e-5	3.e-5	Estimate

3.2. Asymmetric double-cantilever beam

Initially, there was limited money available for experiments, so only two asymmetric double cantilever beam (ADCB) experiments were to be done in order to characterize the mode I interlaminar fracture toughness for a bi-material interface. Each specimen consisted of graphite and glass composite layers cured together with Teflon strips used to create a starter crack. ADCB specimens were fabricated at Sandia, CA, by Tom Bennett, and sent to Kevin Austin at Sandia, NM, for testing. The experimental set-up is shown in Figure 9. Note that hinges were bonded to the specimen ends to facilitate gripping. Also, Figure 10 shows the load-displacement data recorded for the two specimens that were tested.

3.2.1. Optimization

Utilizing the results of the first ADCB experiment, a material parameter characterization was performed using Dakota, a toolkit for optimization, uncertainty quantification, parameter estimation, and sensitivity analysis. This characterization determined the optimum value of the interlaminar fracture toughness using the mechanical properties for the two orthotropic materials determined previously through testing (table 1) and engineering judgment (see [12]). For the traction-separation law, we used the Tvergaard-Hutchinson model with characteristic length scales of 0.05 mm in both normal and tangential directions, and then optimized the critical energy release rate by varying the peak traction. Sensitivity studies showed that the response did not change if the length scale was varied while fixing the critical energy release rate. The optimized interlaminar fracture toughness was determined by Dakota to be 723 J/m^2. The load-displacement data resulting from the ADCB simulation using this fracture toughness is shown in Figure 10. For this optimization, only the data from Specimen 1 was used to determine the optimized fracture toughness value.

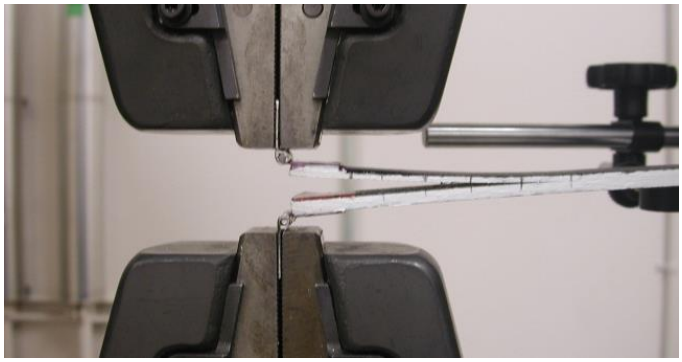

Figure 9: Experimental specimen and fixturing for ADCB.

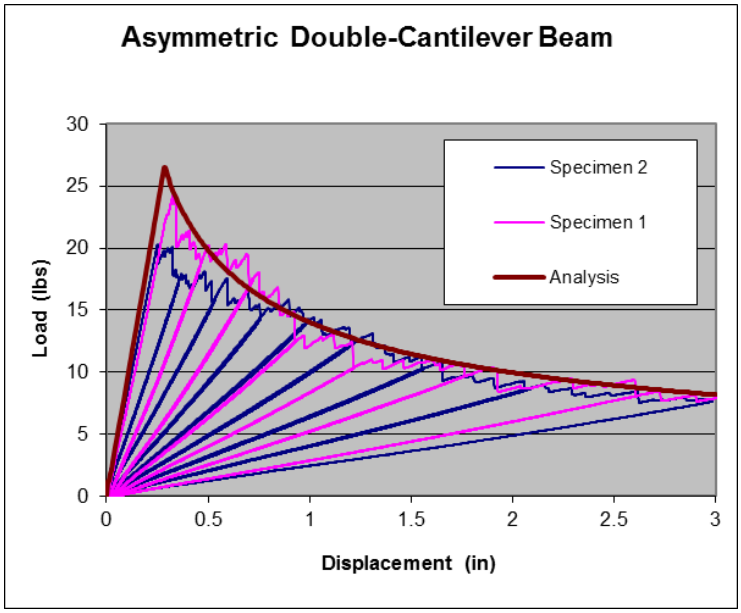

Figure 10: Comparison between simulation and experiment for ADCB.

3.2.2. Discretization verification

Next, a discretization verification was performed on the ADCB simulations. For spatial discretization, three progressively finer mesh sizes, each decreasing in all directions by roughly a factor of 2, were used. The results of the simulations corresponding to these three mesh sizes are shown in Figure 11. Given the three discrete solutions, the observed order of accuracy based on the peak loads was calculated to be $p = 0.87$ with the following equation:

$$\frac{f_3 - f_2}{r_{23}^p - 1} = \frac{r_{12}^p \left(f_2 - f_1 \right)}{r_{12}^p - 1}, \tag{2}$$

where the peak loads, f_i, for the coarse, medium, and fine meshes are $f_3 = 148\,\text{N}$, $f_2 = 144\,\text{N}$, and $f_1 = 140\,\text{N}$, respectively, and the mesh size ratios are $r_{12} = 2$ and $r_{23} = 1.67$. Then, given the value of p, Richardson extrapolation was used to estimate the converged value of the peak load, which is given by $f_{exact} = \frac{f_1 - f_2}{r_{12}^p - 1} = 135.49\,\text{N}$. Alternatively, if the observed order of accuracy, p, is instead calculated with the average force values of $f_2 - f_1$ and $f_3 - f_2$ after the peak, the order of accuracy becomes $p = 1.28$.

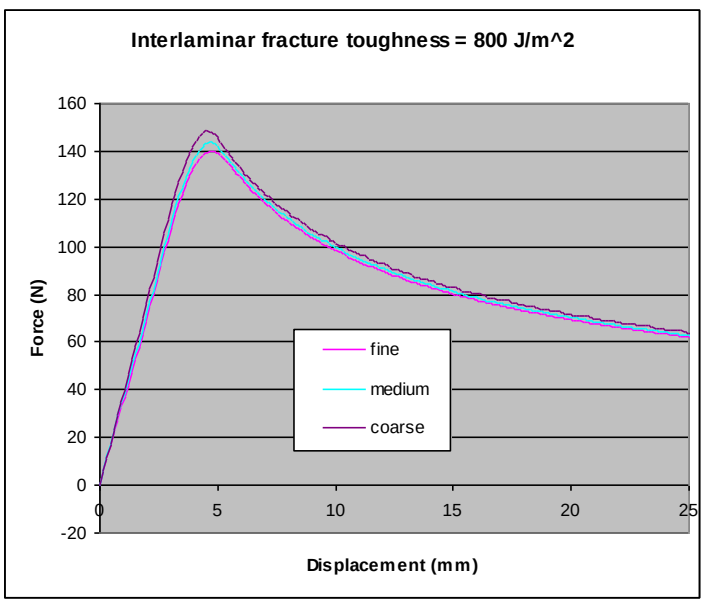

Figure 11: Solution verification for ADCB simulations.

For temporal discretization, ADCB simulations were processed with time steps of 0.02, 0.002, and 0.0002 seconds. There was a difference of less than 1% between the loads for the smaller two time steps (Figure 12).

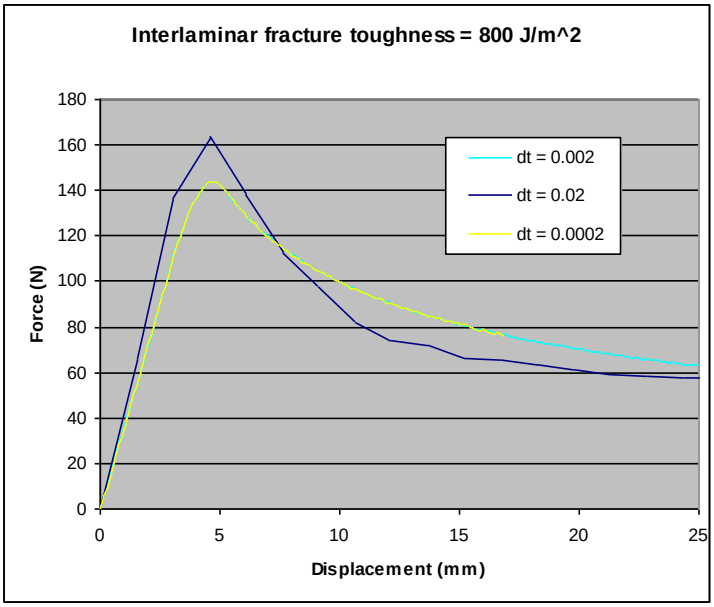

Figure 12: Time discretization convergence study.

3.3. End-notched flexure

The results of end notch flexure experiments, completed with the same bi-material system as the ADCB tests, were used to characterize the mode II fracture toughness. ENF experiments were completed with two orientations. The first orientation tested specimens with the thicker, glass composite layer on top and the second orientation positioned the thinner, graphite layer on top. The test set-up with a specimen oriented in the first position is shown in Figure 13.

Using the same parameter set as the earlier ADCB simulations and an interlaminar fracture toughness of 800 J/m^2, a model of the end notched flexure (ENF) geometry shown in Figure 13 was simulated. The simulation's prediction matched the experimental results very well (see Figure 14). A simulation of the second test orientation (thinner composite layer on top, see Figure 15) was also completed and the analytical results once again matched the experimental results very well (see Figure 16). The difference in the load-displacement curves for the two orientations is due to the residual stress state that results from the specimen fabrication. The thinner composite layer has a lower coefficient of thermal expansion (CTE) than the thicker layer, so as the asymmetric beam is cooled to room temperature from the curing temperature, it curves slightly due to residual stresses that put the interface into shear. In the orientation depicted in Figure 15, the residual shear stress enhances the shearing introduced by the 3-point bending of the beam, whereas in the other orientation, the residual shear stresses at the interface from the CTE mismatch partially counteract the stresses produced by loading.

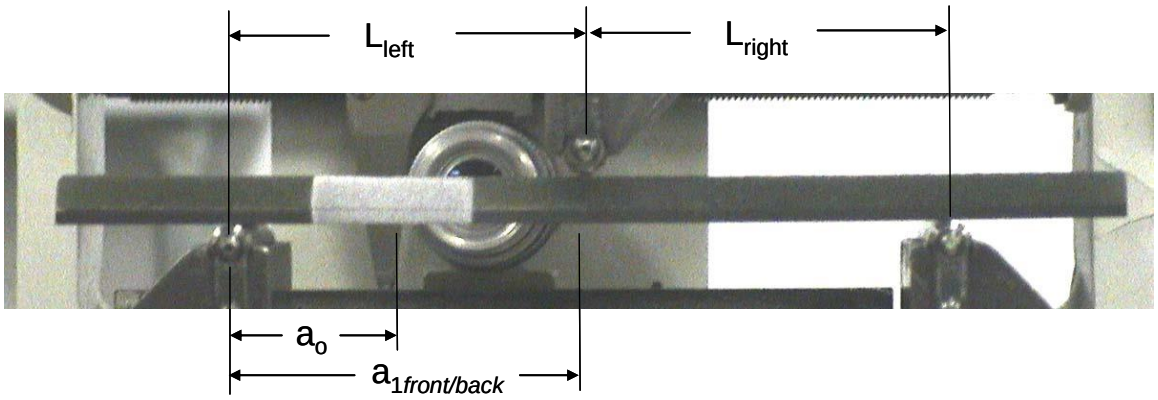

Figure 13: ENF specimen and fixturing.

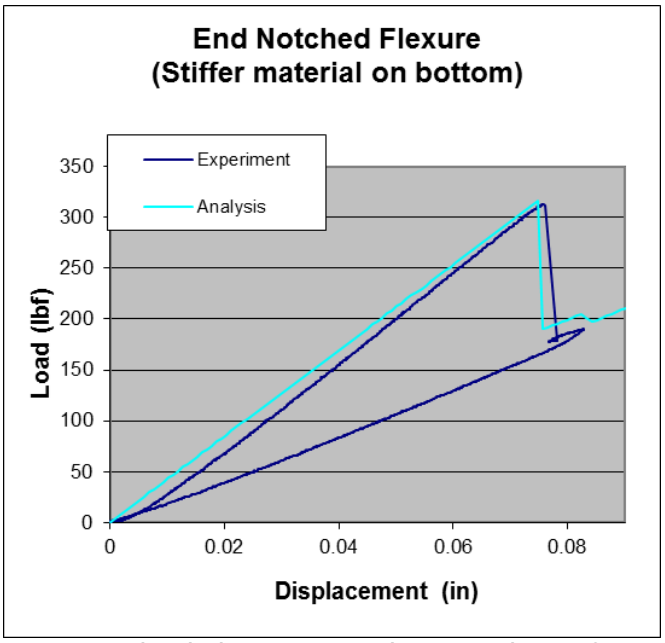

Figure 14: Simulation compared to experiment for ENF.

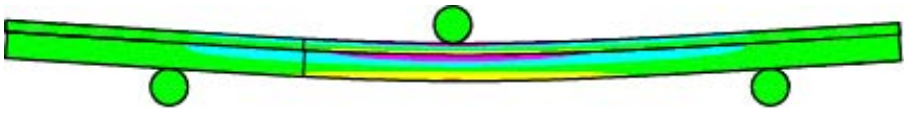

Figure 15: Simulation deflection of ENF geometry.

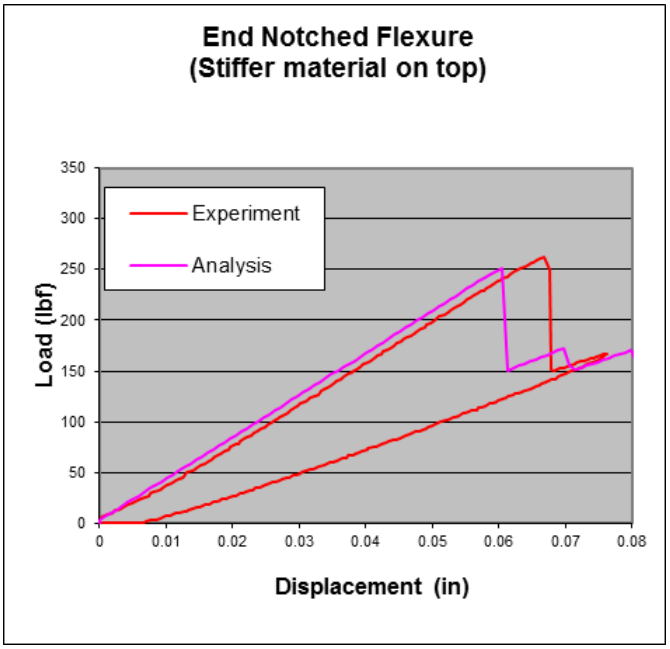

Figure 16: Simulation compared to experiment for ENF.

To verify that these results were not mesh dependent, the ENF model was simulated with three different meshes, consisting of 14798, 113870, and 877406 elements (see Figure 17). The results show that the peak load is extremely insensitive to mesh size. The peak loads for all three meshes were within 1% of each other.

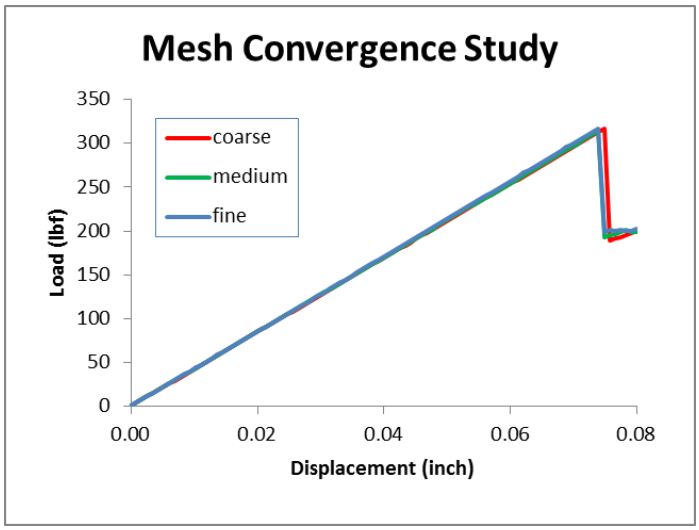

Figure 17: Mesh convergence study for the ENF simulation.

Based on the results in Figure 10 for the ADCB simulation and Figure 14 andFigure 16 for the ENF simulations, it initially appeared as though the interlaminar fracture toughness was roughly the same in both mode I and mode II. This was somewhat surprising, since the critical energy

release rate in mode I is generally considerably lower than the value for mode II. As discussed in Section 3.4, we later found that it was due to material variability. For specimens created at the same time, the mode I critical energy release rate was much lower than the mode II value.

3.3.1. Sensitivity analysis

Also for the end-notched flexure geometry, Dakota was used to run a Latin hypercube sampling (LHS) sensitivity study with 37 geometric and material property parameters to quantify the effect of variability and the assumptions made in determining the composite material properties. Each geometric and material parameter was given a range of +/- 5% of its nominal value. Two response functions, namely maximum load and compliance, were calculated from the results. Correlation matrices and scatter plots were generated using JMP. The full correlation table is too large to be repeated here, but the correlations that are related to the two response functions are provided in Table 2 and the results from the ensemble of simulations are shown in Figure 18.

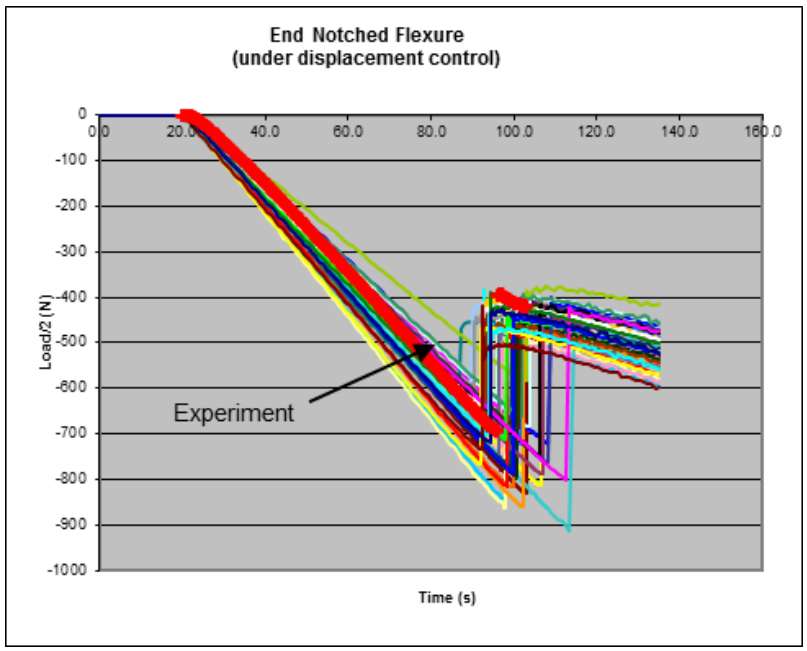

Figure 18: ENF simulation results from the sensitivity analysis.

Both linear and quadratic model fits to each of two response objectives were obtained, and the sensitivity of each term was determined based on a statistical test for whether or not the coefficient of each term in the model fit is zero. Based on the 800 LHS runs, a least-squares fit was computed according to a linear model:

$$G_{IIc} = a_0 + \sum_{n=1}^{N} a_n x_n \tag{3}$$

A depiction of the quality of the fit for Equation (3) is shown in Figure 19. The results of the sensitivity analysis were then used to determine the uncertainty in the critical energy release rate. The approximate uncertainty in each of the parameters, as listed in Table 3, were propagated

through the surrogate model represented in Equation (3) to determine the uncertainty in the critical energy release rate, which was found to be 10% of the nominal value of 800 J/m^2.

Table 2. Correlation table from sensitivity analysis.

	max load (N)	compliance (N/m)
cure_temp	-0.03991	-0.02543
room_temp	0.022389	0.018486
CTEaa_1	0.074286	0.065448
CTEbb_1	0.001438	0.020154
CTEcc_1	-0.02076	0.029892
CTEaa_2	0.048218	0.029026
CTEbb_2	0.017215	0.039107
CTEcc_2	-0.10007	-0.04815
YMaa_1	0.01347	0.125919
YMbb_1	0.07437	0.031602
YMcc_1	0.00517	0.015733
PRab_1	-0.00041	0.036965
PRbc_1	0.013053	0.037972
PRca_1	0.027427	0.005158
SMab_1	-0.0812	-0.09313
SMbc_1	-0.03167	0.02314
SMca_1	0.016319	0.008593
YMaa_2	0.121825	0.207548
YMbb_2	-0.0428	-0.10923
YMcc_2	0.059085	0.044739
PRab_2	-0.02931	-0.05262
PRbc_2	0.041727	0.045844
PRca_2	0.042338	-0.00522
SMab_2	-0.00982	0.051565
SMbc_2	0.073072	0.047466
SMca_2	0.03509	-0.03619
lambda1	0.007006	0.01017
peak_traction	0.046131	-0.02986
frac_toughness	0.091109	0.032404
length	-0.03236	-0.03715
width	0.594959	0.589563
thickness_1	0.007755	0.236683
thickness_2	0.107842	0.265346
precrack	-0.51965	-0.2457
L1	0.611799	0.362969
L2	0.165347	-0.34557
L3	-0.04245	-0.35556
max load (N)	1	0.727848
compliance (N/m)		1

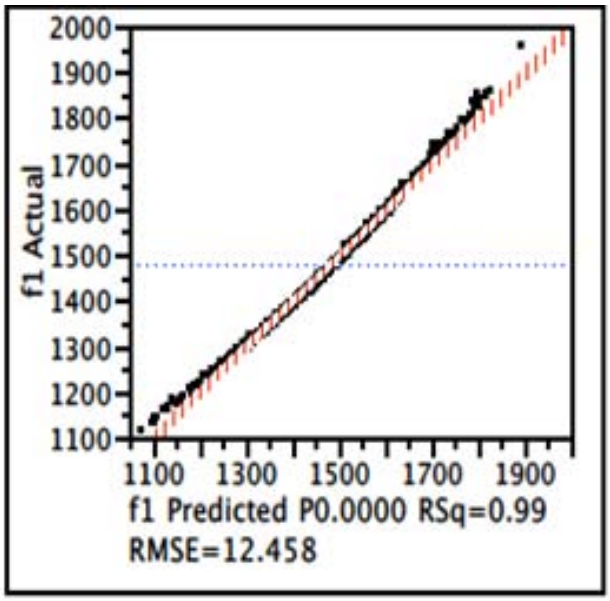

Figure 19: Depiction of the quality of the fit for Equation (3).

Table 3: Nominal values and associated uncertainties for the ENF parameters.

Term	nominal value	UQ +-
cure_temp	450	5
room_temp	294	-5
CTEaa_1	1.00E-06	5.00E-07
CTEbb_1	1.00E-06	5.00E-07
CTEcc_1	3.00E-05	-5.00E-07
CTEaa_2	8.00E-06	5.00E-07
CTEbb_2	8.00E-06	-5.00E-07
CTEcc_2	3.00E-05	-5.00E-07
YMaa_1	6.34E+04	6.34E+02
YMbb_1	5.55E+04	-5.55E+02
YMcc_1	9780	-1.96E+03
PRab_1	0.0782	7.82E-04
PRbc_1	0.303	-0.0606
PRca_1	0.303	0.0606
SMab_1	4612	-4.61E+01
SMbc_1	4612	922.4
SMca_1	4612	922.4

Term	Nominal value	UQ +-
YMaa_2	29189	2.92E+02
YMbb_2	28657	2.87E+02
YMcc_2	10900	-2.18E+03
PRab_2	0.136	-1.36E-03
PRbc_2	0.27	-5.40E-02
PRca_2	0.27	5.40E-02
SMab_2	7766	7.77E+01
SMbc_2	7766	1553.2
SMca_2	7766	1553.2
length	152.4	-0.001
width	25.4	0.003
thickness_1	1.956	0.003
thickness_2	4.521	0.003
precrack	50.8	-0.02
L1	27.973	0.001
L2	49.611	0.001
L3	52.743	-0.001

3.4. ADCB Tests revisited

In general, the critical energy release rate in mode I is lower than the value for mode II. Given the simulation results presented in Figure 10, Figure 14, and Figure 16 it was somewhat surprising that the same toughness value matched experimental results from both mode-I and mode-II experiments. This behavior was possibly explained with composite material variations.

Although the materials and fabrication methods used to manufacture the test specimens were supposedly identical, there was a span of over a year between the production of the ADCB and the ENF specimens, and they were prepared using material plies that were potentially cut from different rolls of pre-preg. To verify this, new ADCB specimens were cut from the same sheets of composite material as the ENF specimens, and then tested. The mode-I critical energy release rate was found to be considerably lower for the new ADCB specimens as compared to the older ones (500 J/m^2 vs 730 J/m^2). This result then raised the possibility that testing method or facility might be playing a role in the discrepancy. To rule this possibility out, some of the older samples were then tested in the SNL/CA test facility using the same methods and experimentalist. It was confirmed that there was no significant difference in measured toughness based on testing facility or tester. This has led to the conclusion that the variation in mode-I toughness between new and old ADCB specimens was due to the age of the pre-preg rolls, as the rolls can partially cure over time during storage, thus changing the interfacial toughness once fully cured.

3.5. High-rate ADCB

A high-rate asymmetric double-cantilever beam test was conducted by Wei-Yang Lu, in which the hinge attached to the top beam to facilitate gripping was held fixed, while the bottom hinge was displaced downwards at a rate of 100 in/s (see Figure 20). During the test, a crack propagation gage measured the crack length as a function of time. This experiment was simulated using Presto, the SIERRA/SM transient dynamics tool (see Figure 21). The initial simulations using the fracture toughness value determined with the quasistatic results (Section 3.2) under-predicted the crack length. The critical energy release rate that fit the crack length data for the high-rate ADCB test was determined to be 250 J/m^2.

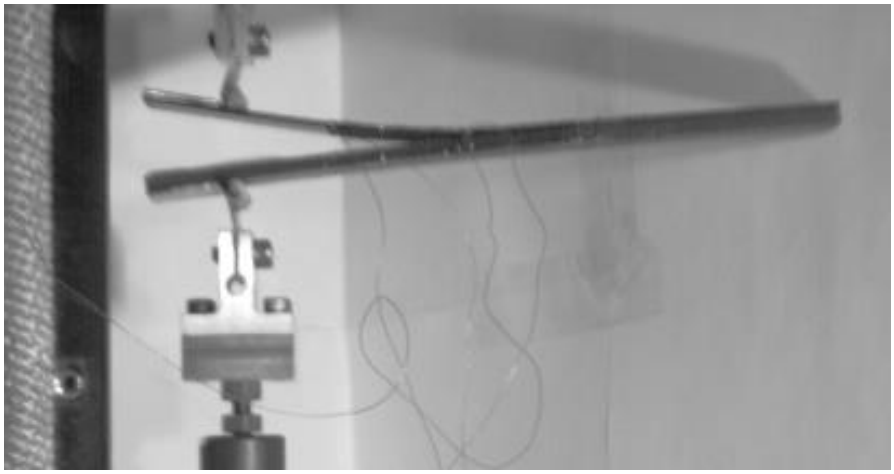

Figure 20: The high-rate ADCB specimen during the fracture test.

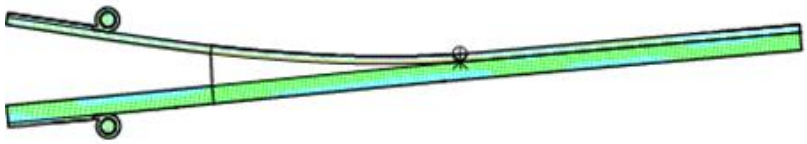

Figure 21: The high-rate simulation showing crack propagation.

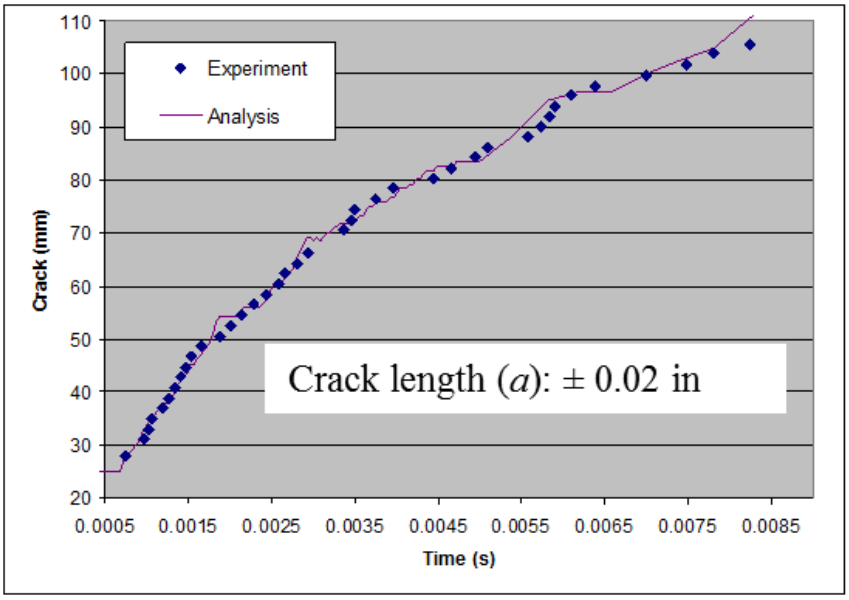

Figure 22: The crack length evolution from simulation and experiment.

3.6. Rising Resistance Curve

Asymmetric double-cantilever beams tests were conducted with specimens that were not pre-cracked. Simulations of these experiments have indicated that the load-displacement response cannot be accurately modeled using a single value for the critical energy release rate. For example, a critical energy release rate of 500 J/m^2 over-predicts the load at first, then under-predicts the load at larger displacements (see Figure 23). This is thought to be due to a rising resistance curve (R-curve), for which the critical energy release rate increases with crack length. For an ideally brittle material, the R-curve is flat. A rising R-curve can occur at composite interfaces due to fiber bridging, as shown in Gregory and Spearing (2004). Significant fiber bridging was also observed for 8-harness, 3k carbon fiber reinforced polymer specimens in Briggs (2012). Another possibility is that microcracks may be dissipating energy on other interfaces in the specimen. This idea is supported by the fact that cracks on other interfaces were observed in some of the ADCB specimens (see Figure 24).

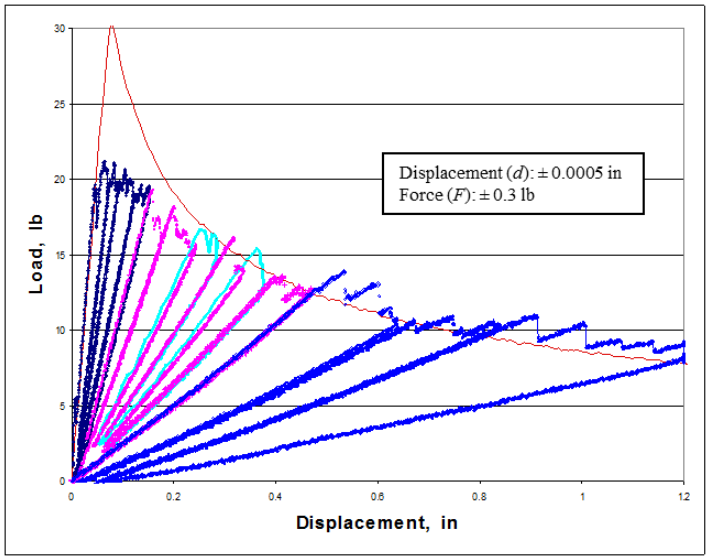

Figure 23: ADCB response without precracking.

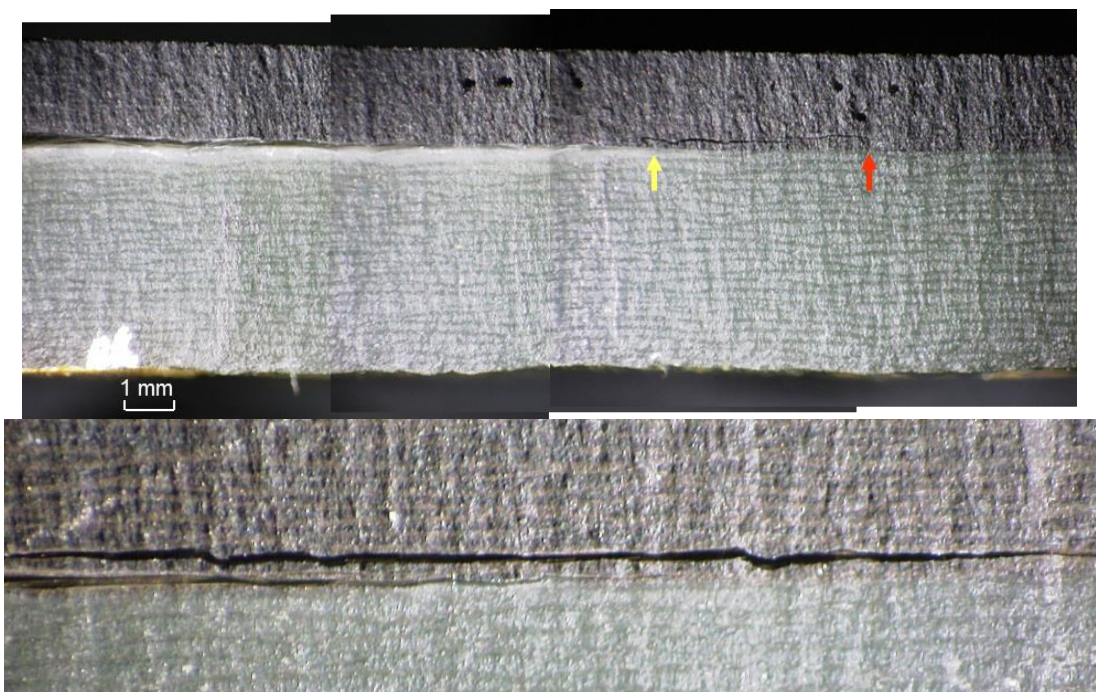

Figure 24: In some ADCB specimens, a secondary crack appeared ahead of the interface crack. The secondary cracks always occurred as delamination between carbon plies.

A relation based on beam theory was derived for the critical energy release rate as a function of load and displacement for a propagating crack (see Appendix):

$$G = \left[\frac{9P^4 d^2}{8b^3} \left(\frac{1}{E_1 I_1} + \frac{1}{E_2 I_2} \right) \right]^{1/3} \tag{4}$$

Using this relation, the critical energy release rate was calculated as a function of crack length and plotted in Figure 25. The corresponding load-displacement curve using this R-curve is shown in Figure 26.

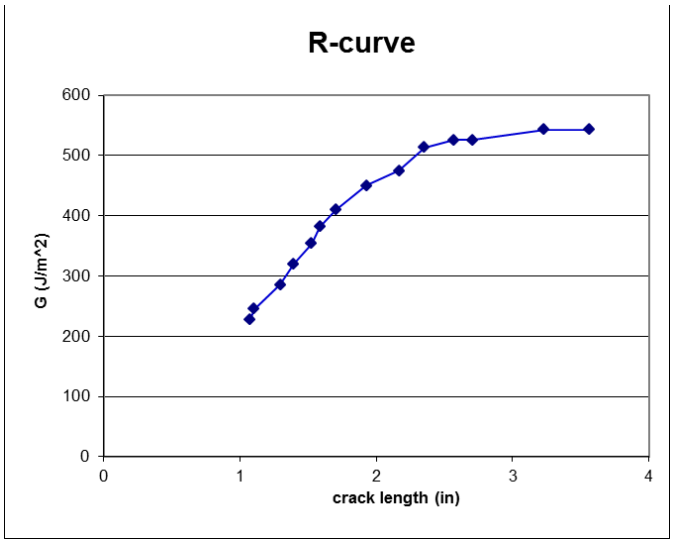

Figure 25: The resistance curve based on Equation (4).

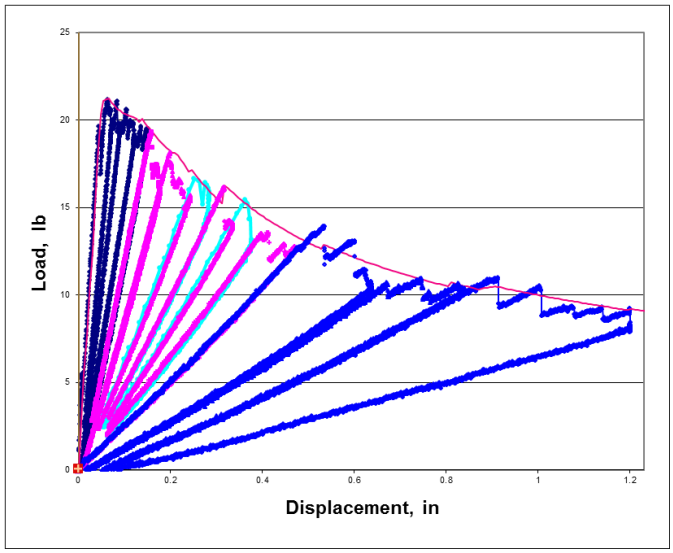

Figure 26: Load-displacement response using the R-curve in Figure 25.

The possibility of modeling the appearance of secondary cracks was investigated. Meshes were created with cohesive surface elements in between the glass and carbon plies on either side of the precracked interface. Each ply between cohesive surface elements had at least three elements through the thickness. Simulations were performed in which the interface between the glass and graphite beams had a critical energy release rate of 250 J/m^2. In one simulation, the interply (i.e. glass-glass and graphite-graphite interface) critical energy release rate had the same value, 250 J/m^2 (see Figures 25 and 26). In this case, no secondary crack forms. In another simulation,

a lower critical energy release rate, 150 J/m^2, was used for the interply interfaces. For this case, a second crack forms between two graphite plies, ahead of the crack at the glass-graphite interface.
It is interesting that the lower interply critical energy release rate actually leads to a higher peak in this case, since more energy is dissipated due to the formation of the secondary crack.

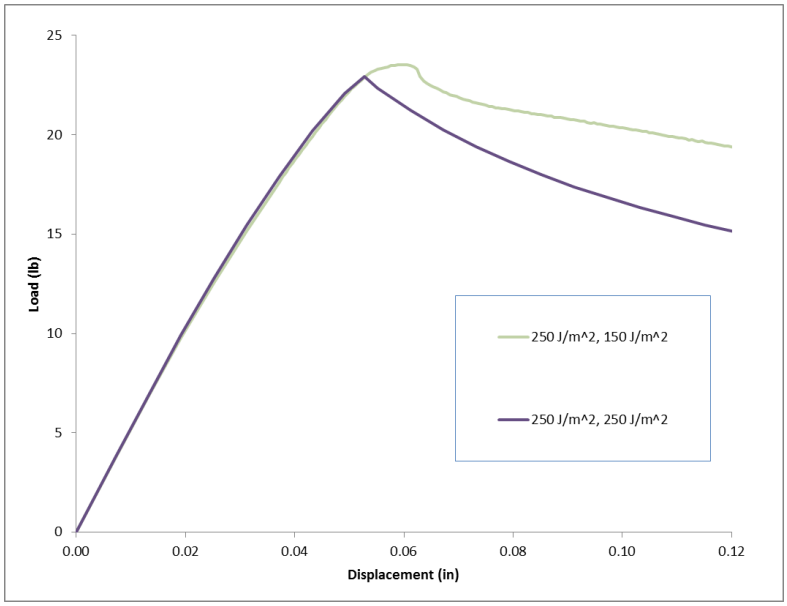

Figure 27: Response curves for the cases where the interply toughness is less than (150 J/m^2) or equal to (250 J/m^2) the interface toughness between the two materials.

Figure 28: Displacements (magnified by 10) at the corresponding peak loads for the cases where the interply toughness is less than (150 J/m^2) or equal to (250 J/m^2) the interface toughness between the two materials.

In simulations, either the secondary crack formed at the beginning of the simulation or it did not form at all. This is in contrast to the experimental specimens, which exhibited significant primary crack growth before a second crack ever formed. Also, the secondary cracks never formed in the older specimens that had been produced first. It is postulated that the simulations have idealized geometries with smooth interfaces, whereas the actual specimens have undulations at each interface since the composite plies are 8-harness satin weaves. Due to the complexity of the material interfaces, we chose to model the mixed mode simulations with a single interface of cohesive surface elements and to treat the critical energy release rate as an

uncertain input parameter that varies from the lower value at crack initiation in mode I to an upper value corresponding to mode II, as described in the next section.

3.7. Validation with Mixed-Mode Flexure

Lastly, MMF experiments were completed and simulated for validation. Mixed-mode flexure specimens were cut from the same cured composite sheets as the ENF and newer ADCB specimens and tested with the fixturing arrangement show in Figure 29. For simulation, the intention was to use the mode-I and mode-II toughness values, previously determined from the ADCB and ENF models, in the Thouless-Parmigiani cohesive zone model, and predict the mixed-mode flexure response. To this end, simulations were attempted using mode I and mode II toughnesses of 250 J/m^2 and 800 J/m^2, respectively, with characteristic length scales of 0.05 mm in both normal and tangential directions. In practice, it proved too difficult to achieve convergence in these simulations using the SIERRA/SM quasistatics code. The best results are shown in Figure 30. The simulation matches the initial compliance well, but then predicts a sharp drop-off in load, which may be due to the solver issues.

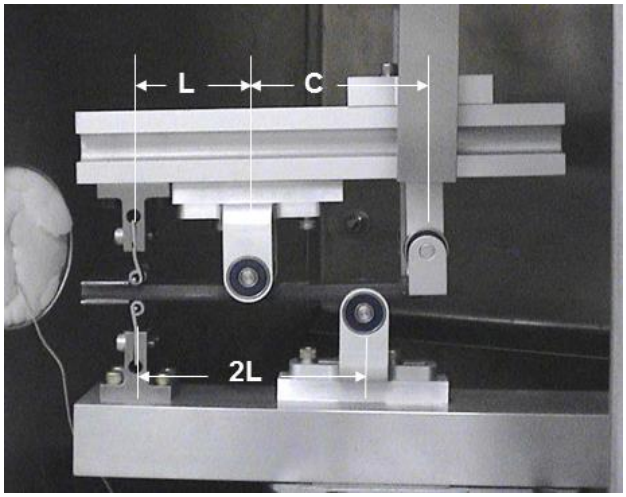

Figure 29: Mixed-mode flexure geometry.

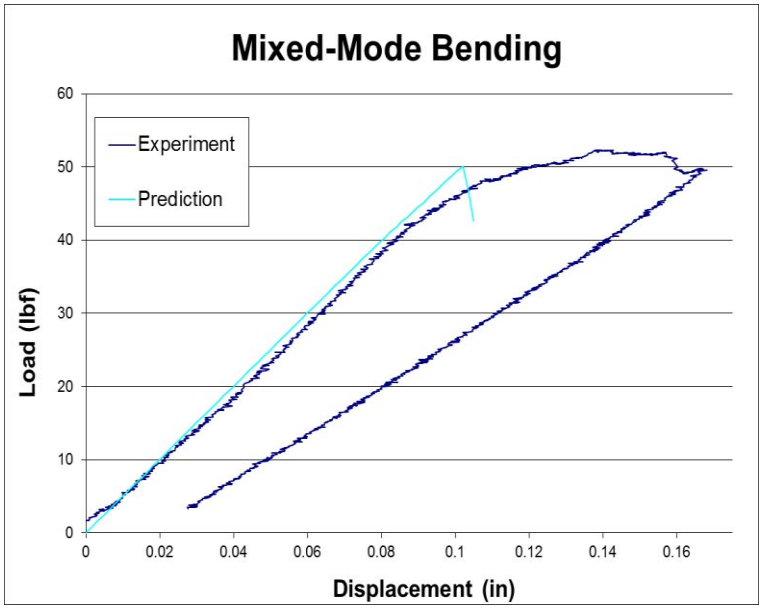

Figure 30: Thouless-Parmigiani model results.

In the end, the Tvergaard-Hutchinson model, which does not account for mode mixity in its toughness value, was used instead. The critical energy release rate was treated as an uncertain input variable with an epistemic range based on the mode-I value as the lower bound and the mode-II value as the upper bound. The results are shown in Figure 31. The large size of the uncertainty bounds in the failure load predictions is mainly due to the uncertainty in the critical energy release rate, which could be as low as 250 J/m^2 for mode I initiation and as high as 800 J/m^2 for mode II propagation.

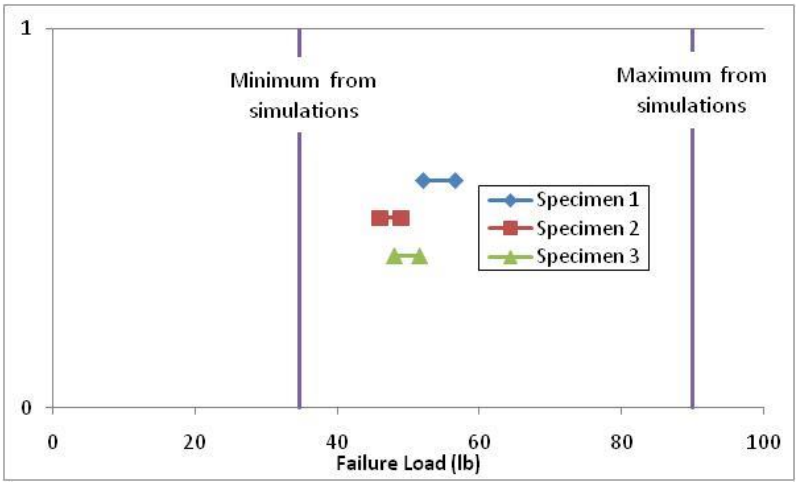

Figure 31: Epistemic uncertainty bounds predicted through simulation, compared with experimental results.

The critical energy release rate for the mixed-mode flexure geometry was estimated using the Tvergaard-Hutchinson model to be roughly 580 J/m^2 for a sample that had not been precracked, and 700 J/m^2 for a precracked sample (see Figure 32 and Figure 33, respectively).

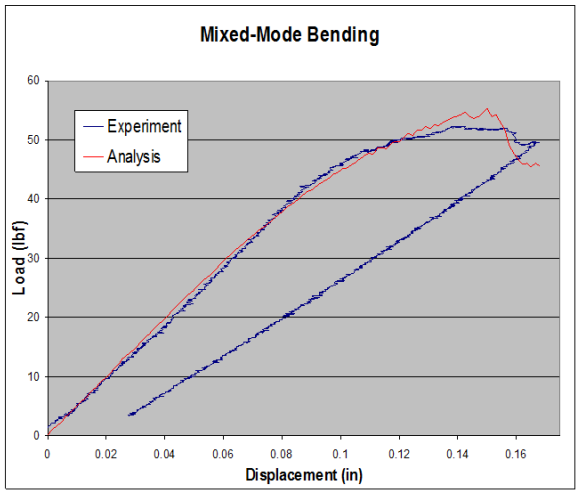

Figure 32: Mixed-mode flexure results for 580 J/m^2.

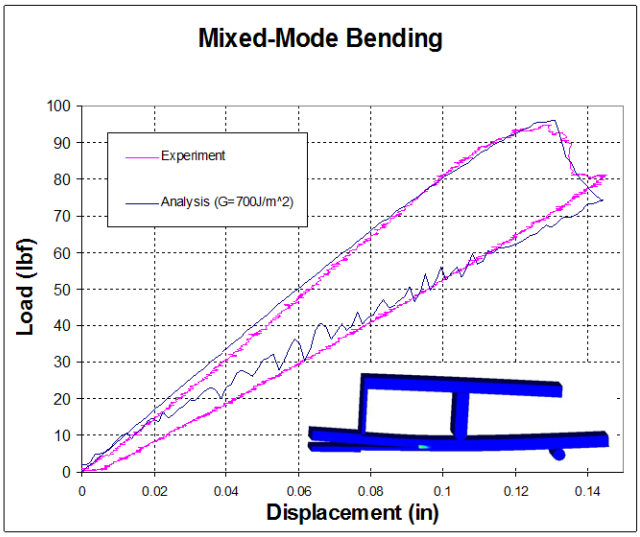

Figure 33: Mixed-mode flexure results for 700 J/m^2.

4. SUMMARY AND CONCLUSIONS

Cohesive surface elements were used to model crack initiation and propagation along predefined paths. Mesh convergence was observed with SIERRA/SM for numerous geometries. Code verification was performed to compare code predictions to analytical solutions for simple three-element simulations as well as a higher-fidelity simulation of a double-cantilever beam. Parameter identification was conducted using experimental results on asymmetric double-cantilever beam (ADCB) and end-notched-flexure (ENF) experiments conducted under Campaign-6 funding. Mixed-mode flexure experiments were simulated for validation.

A rising resistance curve was observed in the ADCB experiments. It is assumed that the increased critical energy release rate with crack length is due to fiber bridging, microcracking, and the formation of secondary cracks due to delamination in between graphite plies.

One of the unexplained issues encountered was material property variability for ostensibly the same composite material. It is believed that the variation in mode-I toughness between new and old ADCB specimens was due to the age of the pre-preg rolls, which can partially cure over time in storage, thus affecting the interfacial toughness of the fully cured composite. Since the variability is not fully understood, it makes it difficult to accurately assess uncertainty when performing predictions.

5. REFERENCES

1. Xu, X.P., and Needleman, A. (1993). "Void Nucleation by Inclusion Debonding in a Crystal Matrix," *Mod. and Sim. in Mat. Sci. and Eng.*, Vol. 1, Issue 2, pp.111-132.
2. Tvergaard, V., and J. W. Hutchinson, 1996. "On the Toughness of Ductile Adhesive Joints," *J. Mech. Phys. Solids,* Vol. 44, No. 5, pp. 789-800.
3. Thouless-Parmigiani (2006). "The roles of toughness and cohesive strength on crack deflection at interfaces," *J. of Mech. and Phys. of Solids*, Vol. 54, Issue 2, pp. 266-287.
4. de Moura, M. F. S. F., 2006. *"*Numerical Simulation of the ENF Test for the Mode-II Fracture Characterization of Bonded Joints,*" J. Adhesion Sci. Technol.*, Vol. 20, no.1, pp.37-52.
5. Iannucci, L., 2006. "Dynamic Delamination Modelling Using Interface Elements," *Computers & Structures* Vol. 84, Issues 15-16, pp. 1029-1048.
6. Mi, Y., M. A. Crisfield, G. A. O. Davies and H. B. Hellweg, 1998. "Progressive Delamination Using Interface Elements," *Journal of Composite Materials*; Vol. 32, pp.1246-1272.
7. Liu, S., Y. Mei, and T. Y. Wu, 1995. "Bimaterial Interfacial Crack Growth as a Function of Mode-Mixity," *IEEE Transactions - Part A*, Vol. 18, No. 3, pp.618-626.
8. Wei-Yang Lu (2008). "Characterizing Delamination of a Bi-material Composite." C6 Technical Report.
9. Brown, A.A. and English, S.A. (2012). "Modeling Support for Reentry Systems Transformation," SAND2012-9241.
10. T.L. Anderson, *Fracture Mechanics*, 3rd edition, CRC Press, Florida, 2005.
11. P.A. Klein, J.W. Foulk, E.P. Chen, S.A. Wimmer, and H. Gao, *Physics-based modeling of brittle fracture: cohesive formulations and the application of meshfree methods*, SAND2001-8099, Sandia National Laboratories, Albuquerque, NM, 2001.
12. A.A. Brown, Wei-Yang Lu, James Foulk III, Stephen Margolis, Thomas Bennett, and Yuki Ohashi, *Mode II Fracture – Simulations and Experiments*, SAND2008-4769C, Proceedings of the 23rd Conference of the American Society for Composites.
13. ASTM Standards and Literature References for Composite Materials, 2nd ed, 1990.
14. Gregory, J.R., and Spearing, S.M. (2004). "A fiber bridging model for fatigue delamination in composite materials," *Acta Materialia*, Vol. 52, Issue 19, pp.5493-5502.
15. Timothy M. Briggs (2012), "Developing a Multiscale Test Approach for Characterizing Polymer Composites" SAND2012-7988.

6. APPENDIX

An asymmetric double-cantilever beam with a crack of length a can be considered as two beams (i = 1, 2) that each flex according to

$$d_i = \frac{Pa^3}{3E_i I_i} \tag{5}$$

where

$$I_i = \frac{bh_i^3}{12} \tag{6}$$

is the moment of inertia.

Then by definition, the compliance of the ADCB specimen is given by

$$C \equiv \frac{d}{P} = \frac{d_1 + d_2}{P} = \frac{a^3}{3}\left(\frac{1}{E_1 I_1} + \frac{1}{E_2 I_2}\right). \tag{7}$$

Then

$$G = \frac{P^2}{2b}\frac{dC}{da} = \frac{P^2 a^2}{2b}\left(\frac{1}{E_1 I_1} + \frac{1}{E_2 I_2}\right). \tag{8}$$

Combining the above equations can be combined to deduce the critical energy release rate as a function of the load and displacement:

$$G = \left[\frac{9P^4 d^2}{8b^3}\left(\frac{1}{E_1 I_1} + \frac{1}{E_2 I_2}\right)\right]^{1/3} \tag{9}$$

DISTRIBUTION

1	MS0825	Marty Pilch	1514
1	MS0889	Dave Reedy	1524
1	MS9042	Mary Gonzales	8250
1	MS9042	Michael Chiesa	8259
1	MS9042	Jay Dike	8259
1	MS9042	Nathan Spencer	8259
1	MS9042	Yuki Ohashi	8259
1	MS9042	Stacy Nelson	8259
1	MS9042	Shawn English	8259
1	MS9154	Robert Monson	8244
1	MS9155	Steve Margolis	8954
1	MS0899	RIM-Reports Management	9532 (electronic copy)

Sandia National Laboratories